ACS APPLIED NANO MATERIALS

www.acsanm.org Article

Orientational Switching of Perpendicular Magnetic Anisotropy and Near-Infrared Plasmonic States in $SrRuO_3$ Thin Films: Implications for Spintronic Devices

Jayjit Kumar Dey, Prasanna Das, Sourav Chowdhury, Deepak Prajapat, Daniel Perez-Salinas, Pushpendra Gupta, Garima Kaura, Basanta Roul, Smriti Bhatia, Simranjeet Kaur, Moritz Hoesch, Manuel Valvidares, Kaushik Sen, Bivas Saha, and Sujit Das*

Cite This: https://doi.org/10.1021/acsanm.4c04068 Read Online

ACCESS | Metrics & More | Article Recommendations | Supporting Information

ABSTRACT: The precise manipulation of perpendicular magnetic anisotropy (PMA) and near-infrared plasmonic states holds immense significance for advanced nanoscale spintronics devices including magnetic random-access memory and epsilon-near-zero (ENZ) photonic devices. Notwithstanding the inherent tendency of oxide thin films to favor an in-plane magnetic easy axis, our study unveils an innovative approach to exert experimental control over magnetic anisotropy, magnetic phase in $SrRuO_3$ (SRO) films by growing them coherently and controlling at nanoscale levels via reflection high-energy electron diffraction (RHEED)-assisted pulsed laser deposition (PLD) on distinctively oriented—specifically, (001), (011), and (111) $SrTiO_3$ (STO) single crystalline substrates. Our comprehensive magnetic measurements unequivocally confirm a clear dependence on magnetic anisotropy with more than one competing magnetic phase with different coercivity and saturation magnetization. A larger perpendicular magnetic anisotropy (PMA) is observed for coherently strained SRO films on (001)-oriented STO compared to their counterparts on (011) and (111)-oriented STO. On the other hand, the orientation-dependent SRO films exhibit tunable plasmonic ENZ, increased metallicity, flexible optical conductivity, and customizable optical transparency in the near-infrared region. These results not only provide a straightforward and effective pathway for achieving tunable PMA and transparent plasmonic states in epitaxial oxide layers but also hold the potential to develop state-of-the-art oxide-based optospin−orbit coupled spintronic switching and memory devices.

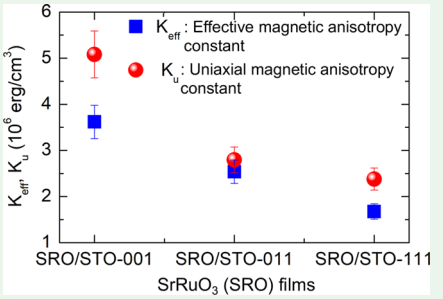

KEYWORDS: *perpendicular magnetic anisotropy, magnetic thin films, spintronics device, plasmonic state, epsilon-near-zero photonic devices*

INTRODUCTION

Perovskite oxide thin films hold a considerable technological promise for spintronic devices such as spin valves, magneto-resistive heads, and magnetoelectric devices[1] as well as for exploring exotic physics like interfacial conduction, magnetism, and superconductivity, over the past decade.[2,3] In oxides particularly transition metal oxides (TMO), have garnered the utmost attention in the research area due to their diverse application possibilities and rich fundamental physics, including the phenomena like the topological Hall effect[4,5] and spin Hall effect.[6] Considering $SrRuO_3$ (SRO) as an example; SRO is an itinerant ferromagnetic metal, widely engaged as an electrode material in the ferroelectric tunneling junctions and field effect transistors,[7] unveiled many exciting phenomena such as magnetic skyrmions,[8] chiral domain walls, Weyl Fermions,[9] large magnetoelastic,[10] tunable magnetic order under strain.[11] The ground state of the SRO magnetic films can be resolved by the competition between magnetic anisotropy and other magnetic interactions like Dzyaloshinskii−Moriya interactions.[12] Especially, perpendicular magnetic anisotropy (PMA) plays a pivotal role in achieving devices with thermal stability and high storage density for magnetic random access memory (MRAM) devices, higher packing densities in storage devices, enhancing the performance of spintronic devices by stabilizing the magnetic orientation, leading to improved read/write speeds and reliability, increased remnant magnetization in the perpendicular direction, and enhanced scalability as well as signal-to-noise ratio for magnetic sensor including position and motion detection. These factors wield significant influence over the power consumption in spin transfer torque (STT) devices, storage density, and data stability of devices.[13−15] On the nanoscale, the manipulation of PMA becomes even more critical. For practical applications,

Received: July 19, 2024
Revised: August 5, 2024
Accepted: August 6, 2024

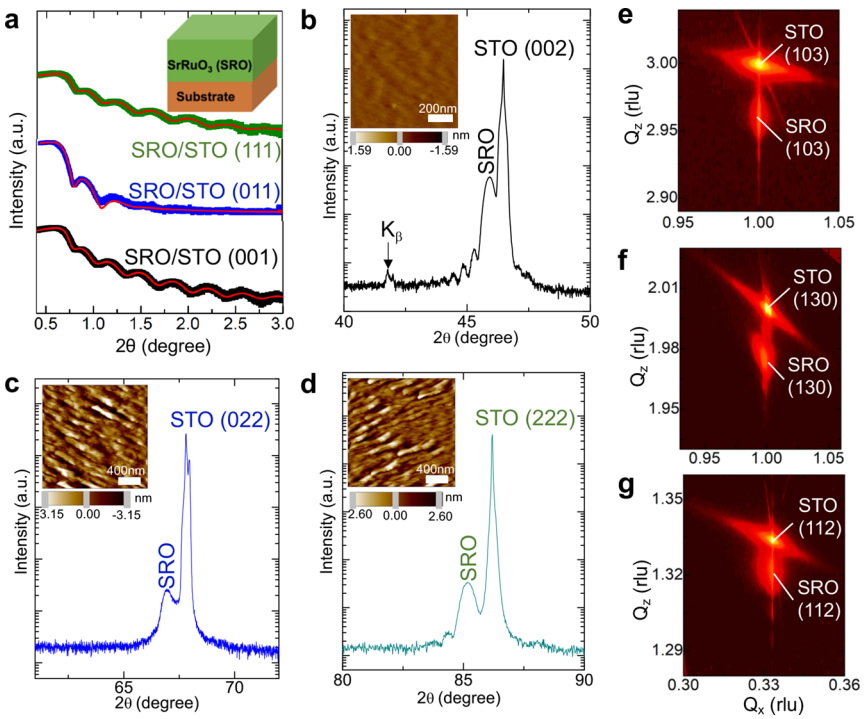

Figure 1. X-ray diffraction (XRD) study of differently oriented SRO films. (a) Low-angle X-ray reflectivity data of films show clear thickness fringes. After fitting the experimental data using the GenX software, we estimated thickness of the films to be ∼27 nm. The fitting is shown by the red lines. Inset: schematic of the composition (SRO) and materials configurations, i.e., SRO grown on differently orientated substrates like (001)-, (011)-, and (111)-oriented STO. $\theta-2\theta$ X-ray diffraction scans (b) around the (002) reflection of the film on STO(001), (c) around the (022) reflection of the film on STO(011) and (d) around the (222) reflection of the film on STO(111). The small peak is the K_β peak coming from the Cu source of the X-ray diffractor. Reciprocal space mapping around the (e) (103) reflection of the film on STO(001), (f) (130) reflection of the film on STO (011), and (g) (112) reflection of the film on STO(111). All films on different orientation are coherently strain after the growth. Atomic force microscopy image of SRO films shows the surface morphology of the film on the (b-inset) STO(100) substrate, (c-inset) STO(011) substrate, (d-inset) STO(111) substrate. All the films show a smooth surface with average roughness ∼3 Å.

materials with strong out-of-plane magnetization are more energetically efficient because it is easier to switch the out-of-plane magnetization (PMA) than in-plane magnetization. Nanoscale features in these materials enhance the control over PMA, enabling precise tuning of magnetic properties and improving the device's performance.

The magnetic anisotropy of SRO is recognized for its complexity; some studies indicate an out-of-plane (oop) easy axis aligned normal to the substrate when subjected to compressive strain and in-plane (ip) direction when subjected to tensile strain.[16,17] While others suggest that the easy axis is dependent on the temperature and the angle to the film normal, the rotation of RuO_6 octahedra by epitaxial strain, thickness, effective Coulomb interaction with dimensionality reduction, buffer/capping layer, and stoichiometry.[18−21] In most magnetic oxide thin films, the magnetic easy axis is mostly aligned along the energetically favorable in-plane orientation because of the demagnetizing energy associated with the out-of-plane orientation. Thus, switching or controlling this magnetic anisotropy is extremely important for applications, although it is challenging. In the same context, Ru-based oxides exhibit mid-infrared optical conductivity, where the kinetic energy of the itinerant electrons and strong spin−orbit coupling control the plasmonic behavior.[22−24] Despite substantial advancements in plasmonic materials research, practical applications remain limited with the main obstacle to widespread utilization closely tied to the inherent properties of these materials. Previous reports claim that bulk SRO possesses optical conductivity in the mid-infrared range, while SRO thin films near-infrared region.[25] There are no reports on the crystal orientational tuning of epsilon-near-zero (ENZ) and its shifting toward the near-infrared wavelength. Additionally, for magnetic materials, especially spin−orbit coupled systems, the manipulation of ENZ is complicated, making it difficult to reveal the basic mechanism of ENZ. ENZ crossover can lead to improved performance in communication systems and infrared sensors, even in surface plasmon resonance (SPR) sensors for detecting biological and chemical substances with high precision. From a crystallographic orientation and spin−orbit coupled magnetic anisotropy standpoint, SRO is certainly encouraging for plasmonic applications, which are still unexplored. An in-depth study based on light-matter interactions in the ENZ frequency regime has laid the foundation of zero-index photonics and revealed a variety of emergent phenomena.[26,27]

Crystallographic symmetry directly links the bond angle and tilting of octahedra,[28−30] which in turn affects the degree of electron correlations. Recently, there has been significant interest in the growth and characterization of (011) and (111)-oriented thin films on the perovskite single crystalline substrates due to their noncubic crystalline surface symmetry.[31−33] However, there has been insufficient attention to the engineered oxide perovskites deposited on (011) and (111)-oriented $SrTiO_3$ (STO) single crystal substrates, primarily due to the challenges associated with epitaxial growth. Through our systematic orientational engineering i.e., by fabricating SRO layers on differently orientated substrates (SRO on STO(001), SRO on STO(011) and SRO on STO(111)), we report the

https://doi.org/10.1021/acsanm.4c04068
ACS Appl. Nano Mater. XXXX, XXX, XXX−XXX

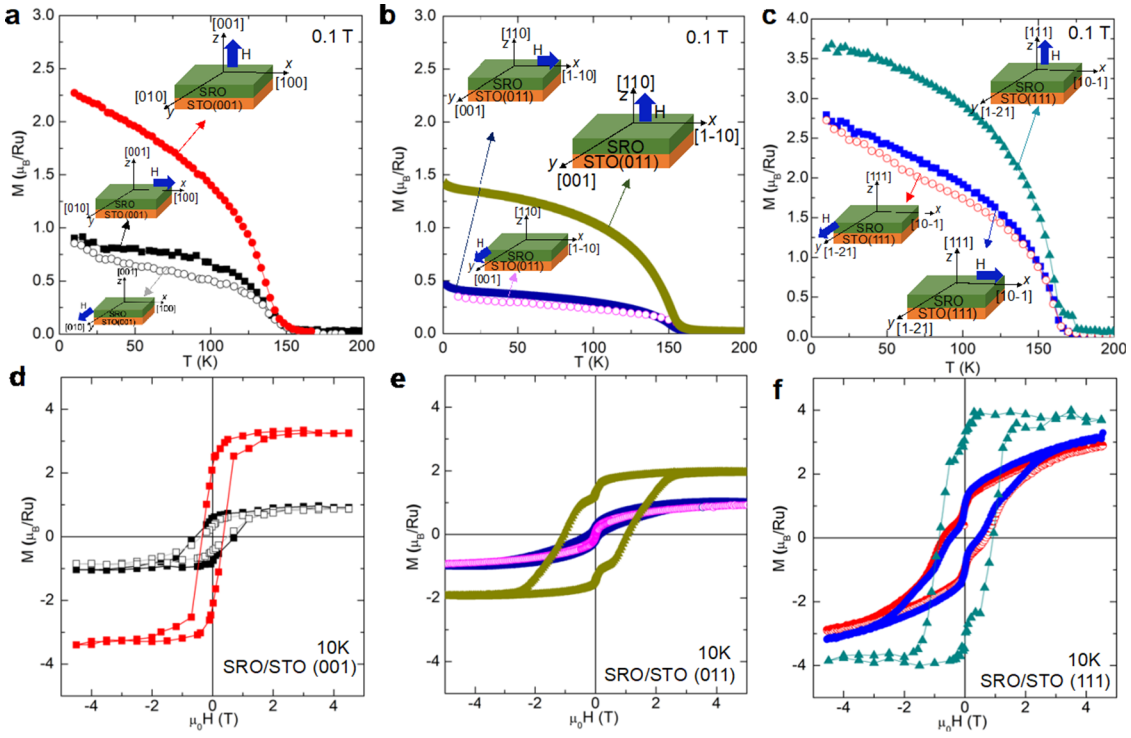

Figure 2. Magnetic anisotropy of the SRO films. (a–c) *M*–*T* curves measured in the warming cycle at 0.1 T magnetic field of the SRO/STO(001) film (a), SRO/STO(011) film (b), and SRO/STO(111) film (c) after field cooling the films at 0.1 T field along both in-plane and out-of-plane directions (measured field direction shown in inset). (d–f) *M*–*H* loops are recorded at 10 K during a magnetic field is applied along the in-plane and out-of-plane directions. The curve is shown after subtracting the high-magnetic-field diamagnetic contribution from the substrates.

manipulation of PMA, multistep magnetic phase, ENZ crossover, and modifiable plasmonic states, particularly ENZ and optical transparency of SRO at the near-infrared wavelength region. We believe our novel approach holds potential for tunable PMA and optoelectronic ENZ in artificially engineered oxide thin films, which is challenging to achieve in the near infrared with conventional plasmonic metals.

EXPERIMENTAL SECTION

The 15 and 27 nm SRO thin films were simultaneously grown on (001), (011), and (111)-oriented single crystalline STO substrate (denoted as SRO/STO(001), SRO/STO(011), and SRO/STO(111), respectively), using the reflection high-energy electron diffraction (RHEED)-assisted multitarget pulsed laser deposition (PLD) technique. During the deposition, RHEED was employed to monitor the growth of the SRO/STO(001) film (Figure S1, composition, and materials configuration are shown in Figure 1a inset). A commercially purchased stoichiometric SRO target was subjected to ablation using a KrF excimer laser (λ = 248 nm) within a deposition chamber equipped with a multitarget carousel to ensure *in situ* deposition of the layers with clean interfaces, with a laser energy density of 1.0 J/cm^2 and a frequency of 10 Hz. The growth took place under controlled parameters such as background oxygen pressure (p_{O2}) of 0.2 mbar and substrate temperature of 700 °C. Subsequent to deposition, an in situ annealing step was performed at 200 mbar oxygen pressure with a temperature of 700 °C for 30 min followed by cooling to room temperature afterward. The crystalline quality and precise thickness of the thin film were checked by X-ray reflectivity using a Bruker D8 Discover diffractometer with Cu-K$_\alpha$ radiation ($\lambda \sim$ 1.5406 Å). The strain states of the epitaxial SRO layers were confirmed by X-ray reciprocal space mapping. The magnetic properties were characterized by using a SQUID (superconducting quantum interference device) magnetometer, measuring along both the out-of-plane and in-plane directions. Samples are cooled from 200 to 10K in the presence of a 0.1 T cooling field, applied parallel and perpendicular to the substrate plane. The magnetic moments were normalized by considering the volume of the sample and average unit cell size for the SRO layer grown on STO, expressed in Bohr magneton per Ru atom. The X-ray absorption spectroscopy (XAS) and X-ray magnetic circular dichroism (XMCD) spectra were measured at the Ru $M_{3,2}$-edge at BOREAS beamline, ALBA synchrotron, Barcelona, Spain in total electron yield (TEY) mode by measuring the sample drain current at 20 K at 6 T magnetic field. The measurements were done at a sample grazing incidence with a sample rotation angle of 20° with respect to both the incident beam and magnetic field by changing the beam helicity at a fixed magnetic field direction. Optical properties were characterized using a state-of-the-art variable angle spectroscopic ellipsometer (J.A. Woollam Co.) in reflection mode at three different incident angles (55°, 65°, and 75°).

RESULTS AND DISCUSSION

Structural Properties. The X-ray reflectivity (XRR) curves exhibit Kiessig fringes throughout the entire thickness of the films, providing clear evidence of well-defined interfaces and a smooth layer structure of the film (Figure 1a). Incorporating the expression for thickness t ($=\lambda/(2\Delta\theta)$), the total thickness of the layers was calculated ~27 nm which is consistent with the X-ray reflectivity fitting. The θ–2θ diffraction patterns are represented near the (002)-reflection for SRO/STO(001), near the (022)-reflection for SRO/STO(011), and near the (222)-reflection for SRO/STO(111), respectively (Figure 1b–d). The peaks corresponding to the SRO films are distinctly visible without any impurity phases, including thickness fringes. This observation indicates the single-phase structure of the films with reasonably smooth interfaces. The positions of the (002), (022), and (222) film peaks provide information about the magnitude of the out-of-

https://doi.org/10.1021/acsanm.4c04068
ACS Appl. Nano Mater. XXXX, XXX, XXX–XXX

plane lattice parameter of the films. The calculated out-of-plane lattice parameters are 3.82 3.96, and 3.92 Å for the SRO/STO(001), SRO/STO(011), and SRO/STO(111), respectively. To comprehend the strain state of the films on differently oriented substrates, reciprocal space mapping at asymmetrical Bragg's reflection was performed (Figure 1e–g). The X-ray diffraction reciprocal space mapping in the vicinity of the (103)-reflection for the SRO/STO(001), the (130)-reflection for the SRO/STO(011), and the (112)-reflection for the SRO/STO(111) (Figure 1e–g) confirms the coherent growth of the layers on each substrate. In other words, the SRO layers exhibit an identical in-plane lattice parameter to that of the respective substrates after the growth. Atomic force microscopy (AFM) images of the SRO/STO(001), SRO/STO(011), and SRO/STO(111) films reveal an average root-mean-square (RMS) roughness of ∼3 Å for the films (inset: Figure 1b–d), indicating an atomically smooth surface for each of them.

Magnetic Properties and Tuning of Magnetic Anisotropy. To unveil the strong dependence of magnetic anisotropy (MA) on substrate orientation, magnetization was measured in all three crystallographic directions of the SRO films (Figure 2). The MA of SRO films exhibits a significant dependence on the growth orientation of the film. The assessments involved applying an external magnetic field in both in-plane (ip) and out-of-plane (oop) directions, using an SQUID magnetometer (Figure 2). The magnetization measurement was performed as a function of temperature ($M-T$) in the presence of a magnetic field of 0.1 T applied both along in-planes and out-of-plane direction of the films after field-cooling (FC) at 0.1 T (field direction shown by blue arrow in the schematic of Figure 2a–c). The onsite spontaneous magnetization of SRO/STO(011) and SRO/STO(111) exhibits a larger Curie temperature (T_C) compared to SRO/STO(001), while saturation magnetization (M_S) demonstrates a higher value for SRO/STO(111). The T_C in SRO/STO(111) occurs at ∼165 K, and in SRO/STO(011) occurs at ∼150 K, while such transitions occur at a relatively lower temperature of ∼140 K for SRO/STO(001) (Figure 2a–c). This enhancement of T_C in SRO/STO(011) and SRO/STO(111) is attributed to internal strain developed between the substrate and SRO layers due to lattice mismatch and shear strain as compared to earlier reports.[34] This strain may lead to a change in the Ru–O–Ru bond angles and/or Ru–O bond lengths, which influences the overlapping of Ru t_{2g} and O 2p orbitals.[11,16,35,36] Notably, the magnetization values in the out-of-plane cases consistently surpass those in the in-plane cases. This observation implies a preferential alignment of spins along the film's out-of-plane direction, indicating a PMA. Moreover, the magnetization difference between out-of-plane and in-plane direction is consistently higher for the SRO/STO(001) compared to the SRO/STO(011) and SRO/STO(111) films, emphasizing the strong dependence of magnetic anisotropy on the film's growth orientation. The nuanced evolution of magnetic anisotropy is further characterized by a field-dependent magnetization hysteresis ($M-H$) at 10 K (Figure 2d–f).

The $M-H$ hysteresis loops for the SRO/STO(001), SRO/STO(011), and SRO/STO(111) films were recorded at temperature T = 10 K after field-cooling (FC) the samples under a 0.1 T magnetic field along both in-plane and out-of-plane directions of the samples (Figures 2d–f and 3a–c). It is evident that the $M-H$ hysteresis loop (in-plane and out-of-plane) symmetries are notably different among the SRO/STO(001), SRO/STO(011), and SRO/STO(111), respectively. Specifically, the magnitude of M_S is higher in the case of SRO/STO(111) compared with the SRO/STO(001) and SRO/STO(011) samples. The saturated moment along the in-plane direction of the SRO/STO(001), SRO/STO(011), and SRO/STO(111) is found to be 0.7 μ_B/Ru at 3.5 T, 0.9 μ_B/Ru at 5.0 T and 3.0 μ_B/Ru at 4.5 T, respectively. The saturated moment along the out-of-plane direction of the SRO/STO(001), SRO/STO(011), and SRO/STO(111) is 3.3 μ_B/Ru at 2.5 T, 1.9 μ_B/Ru at 2.5 T and 3.8 μ_B/Ru at 2.2 T. In contrast to the SRO/STO(011)-oriented films, the SRO/STO(001) and SRO/STO(111) films exhibit higher out-of-plane saturated moments.[37] This also indicates clear magnetic anisotropy for all of the samples. More importantly, the out-of-plane saturated magnetic moment is ∼79% higher than the in-plane saturated magnetic moment for the SRO/STO (001), signifying the robust PMA for the SRO/STO(001), while it is ∼52% higher for the SRO/STO(011) and ∼21% higher for the SRO/STO(111), signifying the moderate PMA for the SRO/STO(011) and lower PMA for the SRO/STO(111). The double-step magnetization observed in the MH curves (Figure 2e,f) suggests the multiple competing magnetic phase/canted spin orientations with different coercivities and saturation magnetizations. The relative contributions of these magnetic phases vary with the substrate orientations, resulting in differences in saturation magnetization among the SRO/STO(001), SRO/STO(011), and SRO/STO(111) films. This variation is attributed to the relative contributions of the magnetic phases within the thin films rather than changes in the Ru spin state, as will be discussed in the XMCD section.

To delve deeper into the influence of the growth orientation of the films on PMA, the uniaxial anisotropy constant (K_u) has been calculated at 10 K using the formula[38]: $K_u = K_{eff} + 2\pi M_s^2$;

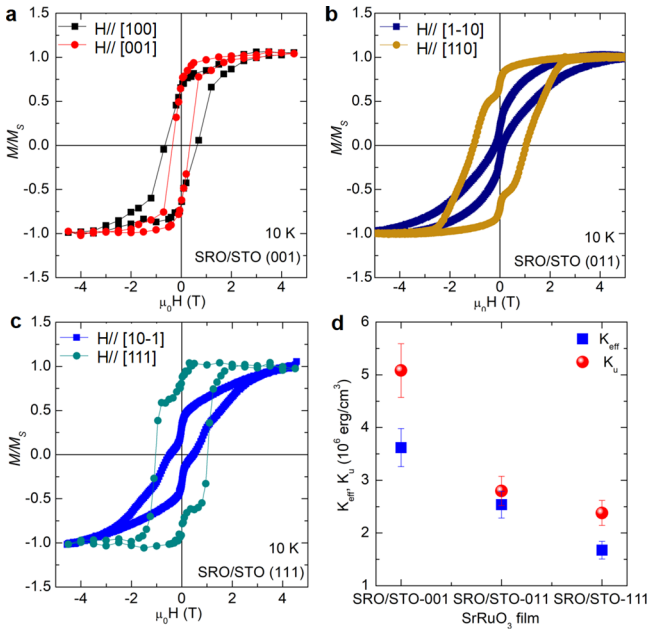

Figure 3. Orientation-dependent anisotropy constant of SRO films. (a–c) Normalized $M-H$ loop at 10 K of the SRO/STO(001) film (a), SRO/STO(011) film (b), and SRO/STO(111) film (c). (d) Calculated effective magnetic anisotropy constant (K_{eff}) and uniaxial magnetic anisotropy constant (K_u) of the differently oriented SRO films.

https://doi.org/10.1021/acsanm.4c04068
ACS Appl. Nano Mater. XXXX, XXX, XXX–XXX

where, $K_{eff} = M_S \cdot H_a/2$ represents the effective anisotropy constant, with M_S and H_a denoting the saturated magnetization and anisotropic field, respectively. The value of H_a is calculated as the difference in saturation fields (H_S) between in-plane and out-of-plane field directions, while $2\pi M_s^2$ represents the demagnetization energy. Notably, the effective anisotropy constant, K_{eff}, is the largest for the SRO/STO(001) film in comparison to those for the SRO/STO(011) and SRO/STO(111) films. This observation underscores a clear dependence of PMA on the growth orientation of the films (Figure 3d). Furthermore, the calculated uniaxial anisotropy (K_u) values reveal that all films exhibit positive K_u values indicating the spin aligns along the out-of-plane direction. Notably, the SRO/STO(001) film demonstrates a pronounced increase in K_u, indicating robust PMA. The growth orientation of the film is evidently a pivotal factor in inducing PMA in SRO epitaxial films. The strong spin−orbit coupling (SOC) of the Ru element promotes a preferential occupancy of the $d_{3z2\text{-}r2}$ orbital of the e_g electrons, leading to PMA. This dependency on growth orientation emphasizes that the latter can effectively enhance shear strain, influencing magnetic anisotropy (MA) and, consequently, varying PMA among the films. Along with magnetocrystalline anisotropy, strong spin−orbit coupling, interfacial effects, and orbital hybridization are responsible for exhibiting the tuning nature of magnetic properties in different oriented films. Interestingly, the magnetocrystalline anisotropy, which is the source of PMA due to spin−orbit coupling, is nothing but proportional to the difference between the out-of-plane and in-plane orbital magnetic moment for 3d transition metals as proposed by Bruno.[39] Although SRO is a strong spin−orbit coupled system, bulk SRO has very little orbital magnetic moment.[40] If the Bruno theory holds for Ru-based 4d compounds, SRO/STO is anticipated to exhibit a finite orbital magnetic moment in the direction perpendicular to the film plane.

To realize the stability of the magnetic ground state of an SRO, it is crucial to control its magnetic properties. A detailed elemental magnetization study was performed at the Ru $M_{3,2}$-edge XMCD for all the films at 20 K at a 6 T magnetic field (Figures 4 and S2). The variation of the XMCD signal is consistent with the magnetometry results among the films. An energy shift of ∼2 eV is observed at the M_3 edge XAS and XMCD maxima in all the films, consistent with earlier reports.[37] This shift can be explained by considering that only the t_{2g} orbitals contribute to the XMCD signal, whereas both the t_{2g} and e_g orbitals contribute to the XAS spectrum. The maximum in the XAS spectrum corresponds to the unoccupied e_g levels. Therefore, this energy difference indicates the crystal-field splitting ($10Dq$) between the t_{2g} and e_g orbitals, which is ∼2 eV. This suggests a ground state configuration of $t_{2g}^4 e_g^0$ for the Ru^{4+} ion, confirming a low-spin state ($S = 1$) configuration of all the films.[41] For a high spin $S = 2$ state, the XMCD maximum at the L_3 edge would typically occur at a higher photon energy, and the L_3 and L_2 edge XMCD line shapes would be asymmetric. In such a high-spin state ($S = 2$), the separation between the XAS and XMCD maxima should be reduced. However, our experimental results for all orientations do not support this, indicating that the films do not exhibit a high-spin ($S = 2$) state.

Furthermore, we have used the sum rules[42,43] to calculate the orbital magnetic moment (l_Z) and the spin magnetic moment (s_Z) of the films. According to the sum rules, the s_Z and l_Z are given as

$$s_Z = -N^d\left(\frac{6p - 4q}{r}\right); \quad l_Z = -\frac{4}{3}N^d\left(\frac{q}{r}\right)$$

where, $p = \int_{L3}(\mu^+ - \mu^-)\, dE$; $q = \int_{L2,3}(\mu^+ - \mu^-)\, dE$; $r = \int_{L2,3}(\mu^+ + \mu^-)\, dE$; and N^d is the number of holes in the 3d orbital, which we considered as 6. We have fitted an arctangent step background and subtracted it from both the μ^+ and μ^- spectra to exclude the nonmagnetic part. We also analyzed the XMCD spectra using other backgrounds like linear and step functions, however, no noticeable change was observed in calculated moment values. Using the sum rules, the s_Z and l_Z values are found to be 1.43 and 0.04 μ_B/Ru-ion, respectively, which gives total moment, $s_Z + l_Z = 1.47$ μ_B/Ru-ion for SRO/STO(001) thin film. Similarly, the s_Z and l_Z values are found to be 2.69 and 0.07 μ_B/Ru-ion and 1.35 and ∼0 μ_B/Ru-ion for SRO/STO(011) and SRO/STO(111) thin films, respectively, which gives total moment, $s_Z + l_Z = 2.76$ and 1.35 μ_B/Ru-ion for SRO/STO(011) and SRO/STO(111) thin films, respectively.

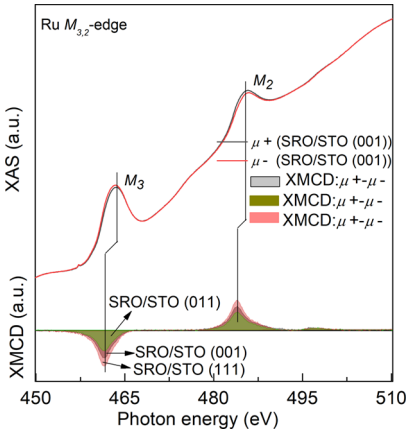

Figure 4. Orientation-dependent elemental magnetization of the SRO films. (Upper part) Ru $M_{3,2}$-edge X-ray absorption spectra measured with fixed magnetic field direction (+6 T) at +Ve helicity (μ^+) and at −Ve helicity (μ^-) in SRO/STO (001) thin film. (Lower part) X-ray magnetic circular dichroism (XMCD) ($\mu^+ - \mu^-$) spectra of all the SRO/STO thin films.

Optical Properties. To gain insight into the optical properties of the SRO films, variable-angle spectroscopic ellipsometry (VASE) is employed to measure the dielectric permittivity of the SRO thin films grown on an STO substrate with three different growth orientations. The dielectric behavior of a material holds paramount significance, complemented by various other optical parameters such as refractive index (n), extinction coefficient (k), and reflectivity (R). Experimentally obtained psi (ψ) and delta (Δ) spectra are fitted with a combination of Drude−Lorentz oscillator model using Complete EASE software to extract the dielectric permittivity, as illustrated in Figure 5. The real part of the dielectric permittivity (ε') exhibits a positive (dielectric)-to-negative (metallic) crossover, known as epsilon-near-zero (ENZ), in the near-infrared region, indicating the onset of metallic (plasmonic) characteristics in the SRO film (Figures 5a and S3). Specifically, for SRO/STO (001), SRO/STO(011), and SRO/STO(111) STO, the ENZ wavelengths are 1160, 1220, and 1110 nm, respectively. The lower ENZ wavelength in the SRO/STO(111) film corresponds to its

https://doi.org/10.1021/acsanm.4c04068
ACS Appl. Nano Mater. XXXX, XXX, XXX−XXX

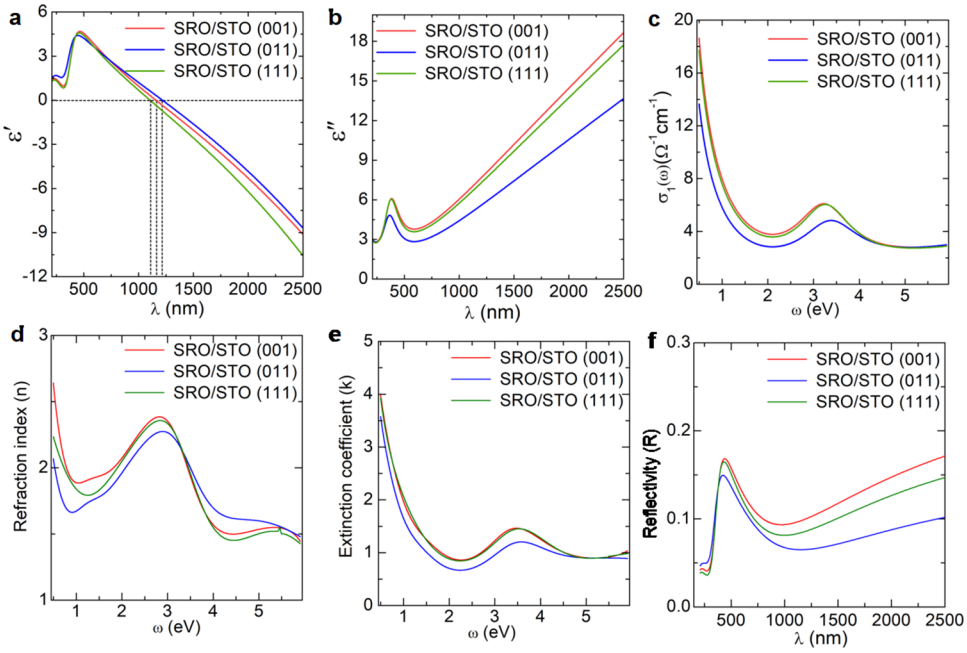

Figure 5. Optical properties of differently oriented SRO films. (a) Real and (b) imaginary part of the dielectric permittivity varies with wavelength of radiation of the SRO/STO(001), SRO/STO(011), and SRO/STO(111) films. Real part of permittivity exhibits positive-to-negative crossover, i.e., epsilon near zero (ENZ) in the near-infrared region, while the imaginary part increases due to intraband transition of free electrons. (c) Optical conductivity. (d) Refractive index and (e) extinction coefficient vs photon energy curve up to 6 eV. (f) Variation of reflectivity (R) with wavelength at differently oriented SRO films.

higher free electron concentration compared to those of the SRO/STO(001) and SRO/STO(011), indicating a blue shift of ENZ, which is a little different for thinner SRO films (Figure S3). In the case of SRO/STO(011), the less negative value of the real part of the dielectric constant within the spectral range suggests a decrease in plasmonic properties, confirming the decrease of the metallic response. In the long-wavelength regime (infrared region), metallicity increases as the negative value of the real part rises. The negative real part is correlated to the plasma frequency (ω_p), which depends on the carrier concentration (n_1) and the effective mass (m^*), as given by the formula: $\omega_p = \sqrt{\frac{n_1 e^2}{\varepsilon_0 m}}$, where e represents the electron charge, and ε_0 denotes the vacuum permittivity. Thus, a higher plasma frequency is observed for the SRO/STO(111) film because of higher carrier concentration, confirming the high metallicity, which may arise due to narrow d-band and less s−d exchange scattering. Here, the imaginary part of permittivity, representing the optical loss of any material, increases in the long-wavelength region due to the enhanced intraband transition of free electrons (Figure 5b). The corresponding Loss function, $LF = -Im[\varepsilon^{-1}(\omega)] = [\varepsilon''(\omega)/(\varepsilon'^2(\omega) + \varepsilon''^2(\omega))]$ is calculated from real (ε') and imaginary (ε'') parts of dielectric permittivity. A maximum loss in energy in LF is seen close to plasma frequency, ω_p with a significant red shift from ω_p. The corresponding redshifts (Table S1) are the signature of damping arising from free carriers of metallic SRO. Hence this plasmon damping or scattering time (τ) is deduced from the equation, $\frac{\hbar}{\tau} = \sqrt{[LF(max)]2 - [\omega_p]^2}$ which estimates τ within (0.67−0.81) femtosecond. Despite these optical losses in the infrared region, it is evident that the SRO film still exhibits a robust metallic response in the near-infrared spectra. Here, the LF spectrum shows one maximum close to zero-crossing of ε' and another at a comparatively higher energy of ~4.5 eV. This may indicate effects such as spin−orbit coupling, phononic, and excitonic effects in addition to plasmon excitations. The exchange splitting energy of SRO is about 0.5 eV and this band splitting due to spin−orbit coupling (SOC) is less compared to the energy between the LF peaks which rule out the effect of SOC. Since the phononic peaks due to electron−phonon coupling arise within 5−125 meV, and the energy range of 1.32−4.5 eV does not fall within this low energy range, there is no possibility of phononic effects. In general, excitonic peaks are sharp and asymmetric and have an energy range below the bandgap, which clarifies the nonexistence of excitonic interactions and the obvious presence of plasmonic excitations in the LF spectrum. However, the SOC of Ru element modifies the electronic band structure by splitting the degenerate electronic states, lifting their degeneracy, and altering the energy dispersion, thus influencing the density of states at the Fermi level. This in turn affects the plasmonic response by modifying the dielectric function.

Now, the optical conductivity is calculated by incorporating the equation, $\sigma(\omega) = -i\frac{\omega}{4\pi}|\varepsilon(\omega)-1|$. The increase in optical conductivity within the 0−2 eV range (Figure 5c) and a Drude-like peak are observed in the region attributed to the localized overlapping states at the Fermi level. A reduction in conductivity close to the 2 eV regions is attributed to a decrease in absorption within those regions, whereas peaks in conductivity (~3.2 eV) are indicative of electromagnetic waves penetrating deeply into the material, resulting in a further increase in conductivity. The conductivity peaks emerging (3.22−3.38 eV) in the UV region are ascribed to the possible interband transitions. Considering the charge conservation, the partial spectral weight integral (W) can be calculated from optical conductivity, $W = \int_{E1}^{E2}\sigma(E)\,dE$, and gives the idea of an effective number of electrons participating in optical

https://doi.org/10.1021/acsanm.4c04068
ACS Appl. Nano Mater. XXXX, XXX, XXX−XXX

excitations within a particular energy range. One region with 0−2 eV and another one with 2−4.5 eV are denoted as W_1 and W_2, respectively (Table S2), where a decrease of W_1 (decrease of the electron) in the Drude region is accompanied by an increase of W_2 in (the available unoccupied states) interband transitions. Now, the knowledge of the refractive index of a material clarifies the extent to which electromagnetic waves can propagate through it. Here, the refractive index is deduced from the equation, $n(\omega) = \left[\frac{\varepsilon_1(\omega)}{2} + \frac{\sqrt{\varepsilon_1^2(\omega) + \varepsilon_2^2(\omega)}}{2}\right]^{1/2}$. The nature of the refractive index (Figure 5d) undergoes almost similar trends with differences in values for all of the SRO films. It shows maxima close to 2.8 eV and subsequently, a decline follows, attributed to the increased reflectivity. The variation in the values of "n" can be ascribed to effective internal reflections, possibly elucidated by photon trapping at grain boundaries as seen from AFM (inset: Figure 1b−d). Significantly, "n" is greater than unity which is linked to the deceleration of photons due to successive interactions with electrons, while the decrease in "n" can be associated with a lower density of states. Now the extinction coefficient (k), is directly linked to the light absorption (α) and may be calculated as $k = \frac{\alpha\lambda}{4\pi}$. The values in Figure 5e indicate higher absorption at lower energy (higher wavelength) at the localized density of states around the Fermi level and thus denote SRO thin films' transparency to light. The reflectivity (R) is calculated following the equation, $R(\omega) = \left[\frac{\sqrt{\varepsilon_1(\omega) + i\varepsilon_2(\omega)} - 1}{\sqrt{\varepsilon_1(\omega) + i\varepsilon_2(\omega)} + 1}\right]$.

In the UV region, reflection (Figure 5f) is minimal due to interband transitions, and again, the reflection spectra show a dip around 1100−1200 nm for all three films, which correspond to the ENZ wavelength of the respective film (plasma resonance). Reflection increases in the infrared region due to increased metallicity (higher negative value of ε'). As the (011) oriented film exhibits low metallicity (Figure 5a), the reflection intensity is lower for the (011) film than for the other two films. Specifically, SRO/STO(111) shows comparatively more transparency in lower energy regions. Thus, the tunable nature of the plasmonic characteristics with film orientation offers an easy and effective pathway to use SRO for energy-selective switching optical devices.

CONCLUSIONS

In summary, epitaxial SRO films were used as a model system to attest to the tailoring of magnetic anisotropy by using growth engineering. We show tuning of the perpendicular magnetic anisotropy of the SRO layer by growing the SRO film on different oriented STO substrates. This approach of anisotropy modification is of a general nature and can be extended easily to other perovskite oxides or strongly correlated materials with similar crystallographic structures. Strain-engineered SRO films exhibit manipulated plasmonic behavior with varying growth orientations, as demonstrated by ENZ crossover and increased metallicity in the near-infrared region, providing the potential for versatile applications in next-generation optical devices. Our results thus open the future possibility of tailoring the perpendicular anisotropy and manipulating plasmonic states in the light of spin−orbit coupling at the nanoscale in multifunctional oxide interfaces and applications starting from spintronic storage devices to the heat-generating nanostructures in the near-infrared spectral range and even to metamaterial-based ideal absorbers that exhibit clear absorption for specific wavelengths, useful in thermal imaging and spectroscopy. Moreover, the scattering of confined plasmonic waves at metal−dielectric interfaces carries transverse spin, offering insights into natural phenomena and quantum entanglement and serving as a potential medium for quantum information transfer.

ASSOCIATED CONTENT

Supporting Information

The Supporting Information is available free of charge at https://pubs.acs.org/doi/10.1021/acsanm.4c04068.

Calculation for plasmon scattering and spectral weight integral of $SrRuO_3$(SRO) deposited in (001), (011), and (111)-oriented $SrTiO_3$(STO); details of the SRO film growth using the RHEED pattern, described in the manuscript; X-ray magnetic circular dichroism (XMCD) of the SRO films on differently oriented STO substrates at 20K; and detailed plasmonic properties of liner SRO layers (15 nm) on differently oriented STO substrates (PDF)

AUTHOR INFORMATION

Corresponding Author

Sujit Das − *Materials Research Centre, Indian Institute of Science, Bangalore 560012, India;* orcid.org/0000-0001-9823-0207; Email: sujitdas@iisc.ac.in

Authors

Jayjit Kumar Dey − *Materials Research Centre, Indian Institute of Science, Bangalore 560012, India*

Prasanna Das − *Chemistry and Physics of Materials Unit and International Centre for Materials Science, Jawaharlal Nehru Centre for Advanced Scientific Research, Bangalore 560064, India*

Sourav Chowdhury − *Deutsches Elektronen-Synchrotron DESY, Hamburg 22607, Germany*

Deepak Prajapat − *Deutsches Elektronen-Synchrotron DESY, Hamburg 22607, Germany*

Daniel Perez-Salinas − *ALBA Synchrotron Light Source, Cerdanyola del Vallès, Barcelona E-08290, Spain;* orcid.org/0000-0002-4641-8387

Pushpendra Gupta − *Materials Research Centre, Indian Institute of Science, Bangalore 560012, India*

Garima Kaura − *Materials Research Centre, Indian Institute of Science, Bangalore 560012, India*

Basanta Roul − *Materials Research Centre, Indian Institute of Science, Bangalore 560012, India; Central Research Laboratory, Bharat Electronics, Bangalore 560013, India*

Smriti Bhatia − *Department of Physics, Indian Institute of Technology Delhi, New Delhi 110016, India*

Simranjeet Kaur − *Department of Physics, Indian Institute of Technology Delhi, New Delhi 110016, India*

Moritz Hoesch − *Deutsches Elektronen-Synchrotron DESY, Hamburg 22607, Germany;* orcid.org/0000-0002-0114-2110

Manuel Valvidares − *ALBA Synchrotron Light Source, Cerdanyola del Vallès, Barcelona E-08290, Spain;* orcid.org/0000-0003-4895-8114

Kaushik Sen − *Department of Physics, Indian Institute of Technology Delhi, New Delhi 110016, India*

https://doi.org/10.1021/acsanm.4c04068
ACS Appl. Nano Mater. XXXX, XXX, XXX−XXX

Bivas Saha − *Chemistry and Physics of Materials Unit and International Centre for Materials Science, Jawaharlal Nehru Centre for Advanced Scientific Research, Bangalore 560064, India; School of Advanced Materials, Jawaharlal Nehru Centre for Advanced Scientific Research, Bangalore 560064, India*

Complete contact information is available at: https://pubs.acs.org/10.1021/acsanm.4c04068

Author Contributions

S.D. designed the experiments. J.K.D, P.G., and G.K. carried out the synthesis. J.K.D., P.D., S.B., S.K., K.S. performed the characterization of the samples. S.C., D.P., M.V., D.P.S. carried out the synchrotron measurements. J.K.D., S.C., and S.D. analyzed the data and cowrote the manuscript. S.D. supervised the research. All authors contributed to the discussions and manuscript preparation.

Notes

The authors declare no competing financial interest.

■ ACKNOWLEDGMENTS

S.D. acknowledges the Science and Engineering Research Board (EEQ/2023/000039) and Indian Institute of Science start-up grant for financial support. J.K.D., P.G. would like to acknowledge IoE-IISc Postdoctoral Fellowship. P.D. and B.S. acknowledge the International Centre for Materials Science (ICMS) and Sheikh Saqr Laboratory (SSL) of Jawaharlal Nehru Centre for Advanced Scientific Research (JNCASR) for support. S.D., S.C., M.H. acknowledge DESY (Hamburg, Germany), PETRA III, beamline P04. S.D. acknowledges the DST-DESY partnership. P.D. and S.S. thank the Council of Scientific and Industrial Research (CSIR) for the fellowship. S.K. acknowledges the UGC fellowship. K.S. acknowledges funding support from the Board of Research in Nuclear Sciences (BRNS) under the YSRP scheme. All authors thank the support from the Central Research Facility of IIT Delhi.

■ REFERENCES

(1) Bibes, M.; Villegas, J. E.; Barthelemy, A. Ultrathin oxide films and interfaces for electronics and spintronics. *Adv. Phys.* **2011**, *60*, 5−84.

(2) Dieny, B.; Speriosu, V. S.; Parkin, S. S. P.; Gurney, B. A.; Wilhoit, D. R.; Mauri, D. Giant magnetoresistive in soft ferromagnetic multilayers. *Phys. Rev. B* **1991**, *43*, 1297−1300.

(3) Ohtomo, A.; Hwang, H. Y. A high-mobility electron gas at the $LaAlO_3/SrTiO_3$ heterointerface. *Nature* **2004**, *427*, 423−426.

(4) Matsuno, J.; Ogawa, N.; Yasuda, K.; Kagawa, F.; Koshibae, W.; Nagaosa, N.; Tokura, Y.; Kawasaki, M. Interface-driven topological Hall effect in 520 SrRuO3−SrIrO3 bilayer. *Sci. Adv.* **2016**, *2*, No. e1600304.

(5) Qin, Q.; Liu, L.; Lin, W.; Shu, X.; Xie, Q.; Lim, Z.; Li, C.; He, S.; Chow, G. M.; Chen, J. Emergence of topological Hall effect in a SrRuO3 single layer. *Adv. Mater.* **2019**, *31*, No. 1807008.

(6) Qiu, Z.; An, T.; Uchida, K.; Hou, D.; Shiomi, Y.; Fujikawa, Y.; Saitoh, E. Experimental investigation of spin Hall effect in indium tin oxide thin film. *Appl. Phys. Lett.* **2013**, *103*, 182404.

(7) Cheng, H.; Liu, Z.; Yao, K. Rectifying behavior in $La_{2/3}Sr_{1/3}MnO_3/MgO/SrRuO_3$ magnetic tunnel junctions. *Appl. Phys. Lett.* **2011**, *98*, 172107.

(8) Wang, L.; Feng, Q.; Kim, Y.; Kim, R.; Lee, K. H.; Pollard, S. D.; Shin, Y. J.; Zhou, H.; Peng, W.; Lee, D.; Meng, W.; Yang, H.; Han, J. H.; Kim, M.; Lu, Q.; Noh, T. W. Ferroelectrically tunable magnetic skyrmions in ultrathin oxide heterostructures. *Nat. Mater.* **2018**, *17*, 1087−1094.

(9) Kar, U.; Singh, A. K.; Hsu, Y. T.; Lin, C. Y.; Das, B.; Cheng, C. T.; Berben, M.; Yang, S.; Lin, C. Y.; Hsu, C. H.; Wiedmann, S.; Lee, W.-C.; Lee, W.-L. The thickness dependence of quantum oscillations in ferromagnetic Weyl metal $SrRuO_3$. *npj Quantum Mater.* **2023**, *8*, 8.

(10) Herklotz, A.; Kataja, M.; Nenkov, K.; Biegalski, M. D.; Christen, H. M.; Deneke, C.; Schultz, L.; Dörr, K. Magnetism of the tensile-strain-induced tetragonal state of $SrRuO_3$ films. *Phys. Rev. B* **2013**, *88*, No. 144412.

(11) Zayak, A. T.; Huang, X.; Neaton, J. B.; Rabe, K. M. Manipulating magnetic properties of $SrRuO_3$ and $CaRuO_3$ with epitaxial and uniaxial strains. *Phys. Rev. B* **2008**, *77*, No. 214410.

(12) Ziese, M.; Vrejoiu, I.; Pippel, E.; Esquinazi, P.; Hesse, D.; Etz, C.; Henk, J.; Ernst, A.; Maznichenko, I. V.; Hergert, F. W.; Mertig, I. Tailoring Magnetic Interlayer Coupling in $La_{0.7}Sr_{0.3}MnO_3/SrRuO_3$ Superlattices. *Phys. Rev. Lett.* **2010**, *104*, No. 167203.

(13) Liu, L.; Qin, Q.; Lin, W.; Li, C.; Xie, Q.; He, S.; Shu, X.; Zhou, C.; Lim, Z.; Yu, J.; Lu, W.; Li, M.; Yan, X.; Pennycook, S. J.; Chen, J. Current-induced magnetization switching in all-oxide heterostructures. *Nat. Nanotechnology.* **2019**, *14*, 939−944.

(14) Ikeda, S.; Miura, K.; Yamamoto, H.; Mizunuma, K.; Gan, H. D.; Endo, M.; Kanai, S.; Hayakawa, J.; Matsukura, F.; Ohno, H. A perpendicular-anisotropy CoFeB−MgO magnetic tunnel junction. *Nat. Mater.* **2010**, *9*, 721−724.

(15) Huang, X.; Sayed, S.; Mittelstaedt, J.; Susarla, S.; Karimeddiny, S.; Caretta, L.; Zhang, H.; Stoica, V. A.; Gosavi, T.; Mahfouzi, F.; Sun, Q.; Ercius, P.; Kioussis, P.; Salahuddin, S.; Ralph, D. C.; Ramesh, R. Novel Spin−Orbit Torque Generation at Room Temperature in an All-Oxide Epitaxial $La_{0.7}Sr_{0.3}MnO_3/SrIrO_3$ System. *Adv. Mater.* **2021**, *33*, No. e2008269.

(16) Wakabayashi, Y. K.; Kaneta-Takada, S.; Krockenberger, Y.; Taniyasu, Y.; Yamamoto, H. Wide-Range Epitaxial Strain Control of Electrical and Magnetic Properties in High-Quality $SrRuO_3$ Films. *ACS Appl. Electron. Mater.* **2021**, *3*, 2712−2719.

(17) Aso, R.; Kan, D.; Fujiyoshi, Y.; Shimakawa, Y.; Kurata, H. Strong Dependence of Oxygen Octahedral Distortions in $SrRuO_3$ Films on Types of Substrate-Induced Epitaxial Strain. *Cryst. Growth Des.* **2014**, *14*, 6478−6485.

(18) Jeong, H.; Jeong, S. G.; Mohamed, A. Y.; Lee, M.; Noh, W. S.; Kim, Y.; Bae, J. S.; Choi, W. S.; Cho, D. Y. Thickness-dependent orbital hybridization in ultrathin $SrRuO_3$ epitaxial films. *Appl. Phys. Lett.* **2019**, *115*, 092906.

(19) Chang, S. H.; Chang, Y. J.; Jang, S. Y.; Jeong, D. W.; Jung, C. U.; Kim, Y. J.; Chung, J. S.; Noh, T. W. Thickness-dependent structural phase transition of strained $SrRuO_3$ ultrathin films: The role of octahedral tilt. *Phys. Rev. B* **2011**, *84*, No. 104101.

(20) Gao, R.; Dong, Y.; Xu, H.; Zhou, H.; Yuan, Y.; Gopalan, V.; Gao, C.; Fong, D. D.; Chen, Z.; Luo, Z.; Martin, L. W. Interfacial Octahedral Rotation Mismatch Control of the Symmetry and Properties of $SrRuO_3$. *ACS Appl. Mater. Interfaces* **2016**, *8*, 14871−14878.

(21) Lu, W.; Yang, P.; Song, W. D.; Chow, G. M.; Chen, J. S. Control of oxygen octahedral rotations and physical properties in SrRuO3 films. *Phys. Rev. B* **2013**, *88*, No. 214115.

(22) Kostic, P.; Okada, Y.; Collins, N. C.; Schlesinger, Z.; Reiner, J. W.; Klein, L.; Kapitulnik, A.; Geballe, T. H.; Beasley, M. R. Non-Fermi-liquid behavior of $SrRuO_3$: evidence from infrared conductivity. *Phys. Rev. Lett.* **1998**, *81*, 2498−2501.

(23) Lee, Y. S.; Yu, J.; Lee, J. S.; Noh, T. W.; Gimm, T. H.; Choi, H. Y.; Eom, C. B. Non-Fermi liquid behavior and scaling of the low-frequency suppression in the optical conductivity spectra of $CaRuO_3$. *Phys. Rev. B* **2002**, *66*, No. 041104.

(24) Lee, J. S.; Lee, Y. S.; Noh, T. W.; Char, K.; Park, J.; Oh, S. J.; Park, J. H.; Eom, C. B.; Takeda, T.; Kanno, R. Optical investigation of the electronic structures of $Y_2Ru_2O_7$, $CaRuO_3$, $SrRuO_3$ and $Bi_2Ru_2O_7$. *Phys. Rev. B* **2001**, *64*, No. 245107.

(25) Braic, L.; Vasilantonakis, N.; Zou, B.; Maier, S. A.; Alford, N. M.; Zayats, A. V.; Petrov, P. K. Optimizing Strontium Ruthenate Thin Films for Near-Infrared Plasmonic Applications. *Sci. Rep.* **2015**, *5*, 9118.

(26) Alam, M. Z.; De Leon, I.; Boyd, R. W. Large optical nonlinearity of indium tin oxide in its epsilon-near-zero region. *Science* **2016**, *352*, 795.
(27) Silveirinha, M.; Engheta, N. Tunneling of Electromagnetic Energy through Subwavelength Channels and Bends using ϵ-Near-Zero Materials. *Phys. Rev. Lett.* **2006**, *97*, No. 157403.
(28) Ning, X. K.; Wang, Z. J.; Zhang, Z. D. Anisotropy of electrical and magnetic transport properties of epitaxial $SrRuO_3$ thin films. *J. Appl. Phys.* **2015**, *117*, 093907.
(29) Moon, E. J.; Balachandran, P. V.; Kirby, B. J.; Keavney, D. J.; Sichel-Tissot, R. J.; Schleputz, C. M.; Karapetrova, E.; Cheng, X. M.; Rondinelli, J. M.; May, S. J. Effect of interfacial octahedral behavior in ultrathin Manganite films. *Nano Lett.* **2014**, *14*, 2509−2514.
(30) Liao, Z.; Huijben, M.; Zhong, Z.; Gauquelin, N.; Macke, S.; Green, R. J.; Van Aert, S.; Verbeeck, J.; Van Tendeloo, G.; Held, K.; Sawatzky, G. A.; Koster, G.; Rijnders, G. Controlled lateral anisotropy in correlated Manganite heterostructures by interface-engineered oxygen octahedral coupling. *Nat. Mater.* **2016**, *15*, 425.
(31) Gibert, M.; Zubko, P.; Scherwitzl, R.; Íñiguez, J.; Triscone, J. M. Exchange bias in $LaNiO_3$-$LaMnO_3$ superlattices. *Nat. Mater.* **2012**, *11*, 195−198.
(32) Wei, H.; Jenderka, M.; Bonholzer, M.; Grundmann, M.; Lorenz, M. Modeling the conductivity around the dimensionality-controlled metal-insulator transition in $LaNiO_3$/$LaAlO_3$ (100) superlattices. *Appl. Phys. Lett.* **2015**, *106*, 042103.
(33) Woo, S.; Choi, H.; Kang, S.; Lee, J.; David, A.; Prellier, W.; Kim, Y.; Kim, H. Y.; Choi, W. S. Surface-orientation-dependent growth of $SrRuO_3$ epitaxial thin films. *Appl. Surf. Sci.* **2020**, *499*, No. 143924.
(34) Terai, K.; Ohnishi, T.; Lippmaa, M.; Kawasaki. Magnetic Properties of Strain-Controlled $SrRuO_3$ Thin Films. *Jpn. J. Appl. Phys.* **2004**, *43*, L227.
(35) Gan, Q.; Rao, R. A.; Eom, C. B.; Garrett, J. L.; Lee, M. Direct measurement of strain effects on magnetic and electrical properties of epitaxial SrRuO3 thin films. *Appl. Phys. Lett.* **1998**, *72*, 978.
(36) Zayak, A. T.; Huang, X.; Neaton, J. B.; Rabe, K. M. Structural, electronic, and magnetic properties of SrRuO3under epitaxial strain. *Phys. Rev. B* **2006**, *74*, No. 094104.
(37) Grutter, A. J.; Wong, F. J.; Arenholz, E.; Vailionis, A.; Suzuki, Y. Evidence of high-spin Ru and universal magnetic anisotropy in SrRuO3 thin films. *Phys. Rev. B* **2012**, *85*, No. 134429.
(38) Hua, E.; Dai, K.; Wang, Q.; Ye, H.; Liu, K.; Zhang, J.; Lu, J.; Liu, K.; Jin, F.; Wang, L.; Wu, W. Highly Tunable Perpendicular Magnetic Anisotropy and Anisotropic Magnetoresistance in Ru-Doped $La_{0.67}Sr_{0.33}MnO_3$ Epitaxial Films. *Chin. Phys. Lett.* **2023**, *40*, No. 077501.
(39) Bruno, P. Tight-binding approach to the orbital magnetic moment and magnetocrystalline anisotropy of transition-metal monolayers. *Phys. Rev. B* **1989**, *39*, 865.
(40) Okamoto, J.; Okane, T.; Saitoh, Y.; Terai, K.; Fujimori, S. I.; Muramatsu, Y.; Yoshii, K.; Mamiya, K.; Koide, T.; Fujimori, A.; Fang, Z.; Takeda, Y.; Takano, M. Soft x-ray magnetic circular dichroism study of $Ca_{1-x}Sr_xRuO_3$ across the ferromagnetic quantum phase transition. *Phys. Rev. B* **2007**, *76*, No. 184441.
(41) Agrestini, S.; Hu, Z.; Kuo, C. Y.; Haverkort, M. W.; Ko, K. T.; Hollmann, N.; Liu, Q.; Pellegrin, E.; Valvidares, M.; Herrero-Martin, J.; Gargiani, P.; Gegenwart, P.; Schneider, M.; Esser, S.; Tanaka, A.; Komarek, A. C.; Tjeng, L. H. Electronic and spin states of SrRuO3 thin films: An x-ray magnetic circular dichroism study. *Phys. Rev. B* **2015**, *91*, No. 075127.
(42) Thole, B. T.; Carra, P.; Sette, F.; van der Laan, G. X-ray circular dichroism as a probe of orbital magnetization. *Phys. Rev. Lett.* **1992**, *68*, 1943−1946.
(43) Chen, C. T.; Idzerda, Y. U.; Lin, H. J.; Smith, N. V.; Meigs, G.; Chaban, E.; Ho, G. H.; Pellegrin, E.; Sette, F. Experimental Confirmation of the X-Ray Magnetic Circular Dichroism Sum Rules for Iron and Cobalt. *Phys. Rev. Lett.* **1995**, *75*, 152−155.

https://doi.org/10.1021/acsanm.4c04068
ACS Appl. Nano Mater. XXXX, XXX, XXX−XXX